Sc^{3+}-promoted O–O bond cleavage of a (μ-1,2-peroxo)diiron(III) species formed from an iron(II) precursor and O_2 to generate a complex with an $Fe^{IV}_2(\mu\text{-}O)_2$ core

Saikat Banerjee,[a] Apparao Draksharapu,[a] Patrick M. Crossland,[a] Ruixi Fan,[b] Yisong Guo,*,[b] Marcel Swart,*,[c,d] and Lawrence Que, Jr.*,[a]

[a] Department of Chemistry and Center for Metals in Biocatalysis, University of Minnesota, Minneapolis, Minnesota 55455, United States

[b] Department of Chemistry, Carnegie Mellon University, Pittsburgh, PA 15213, United States

[c] ICREA, Pg. Lluís Companys 23, 08010 Barcelona, Spain

[d] IQCC & Dept. Chem., University of Girona, 17003 Girona, Spain

Supporting Information

ABSTRACT: Soluble methane monooxygenase (sMMO) carries out methane oxidation at 4 °C and under ambient pressure in a catalytic cycle involving the formation of a peroxodiiron(III) intermediate (**P**) from the oxygenation of the diiron(II) enzyme and its subsequent conversion to **Q**, the diiron(IV) oxidant that hydroxylates methane. Synthetic diiron(IV) complexes that can serve as models for **Q** are rare and have not been generated by a reaction sequence analogous to that of sMMO. In this work, we show that $[Fe^{II}(Me_3NTB)(CH_3CN)](CF_3SO_3)_2$ (Me_3NTB = tris((1-methyl-1*H*-benzo[d]imidazol-2-yl)methyl)amine) (**1**) reacts with O_2 in the presence of base, generating a (μ-1,2-peroxo)diiron(III) adduct with a low O–O stretching frequency of 825 cm^{-1} and a short Fe•••Fe distance of 3.07 Å. Even more interesting is the observation that the peroxodiiron(III) complex undergoes O–O bond cleavage upon treatment with the Lewis acid Sc^{3+} and transforms into a bis(μ-oxo)diiron(IV) complex, thus providing a synthetic precedent for the analogous conversion of **P** to **Q** in the catalytic cycle of sMMO.

Introduction

Dioxygen activation is carried out by nonheme diiron enzymes such as soluble methane monooxygenase (sMMO), ribonucleotide reductase (RNR), fatty acid desaturases, human deoxyhypusine hydroxylase (hDOHH) and others.[1–4] These enzymes are involved in various important transformations such as the conversion of methane to methanol, the conversion of ribonucleotides to deoxyribonucleotides, the desaturation of fatty acids and the selective hydroxylation of the eukaryotic initiation factor 5a. Dioxygen binding to the diiron(II) center gives rise to a peroxodiiron(III) species, as observed for sMMO,[5,6] RNR R2,[7,8] fatty acid desaturases,[9,10] and hDOHH[11–13] that in turn convert to high-valent intermediates that play key roles in enzyme action, such as the diiron(III,IV) species "**X**" in RNR class 1A[14–16] or the diiron(IV) species "**Q**" in sMMO.[17–19]

Various synthetic models have been produced to mimic dioxygen activation steps in nonheme diiron enzymes.[2,3,20] The polydentate ligands used for these models incorporate various nitrogen heterocycles, with pyridine and quinoline donors most often represented. Closer analogs of the histidine ligands in the enzyme active sites are imidazoles and benzimidazoles, but there are only a handful of polydentate ligands with these heterocycles that are reported to form (μ-1,2-peroxo)diiron(III) intermediates.[21–27], and not one has been shown to transform into a higher-valent diiron species. Herein, we present a study of $[Fe^{II}(Me_3NTB)(CH_3CN)](CF_3SO_3)_2$ (**1**)[28] (Scheme 1), which in the presence of DBU (1,8-diazabicyclo[5.4.0]undec-7-ene) reacts with O_2 in MeCN at -40° C to form a (μ-1,2-peroxo)diiron(III) species (**2**). Subsequent treatment of this intermediate with $Sc(OTf)_3$ converts **2** to a diiron(IV) complex **3**, thereby providing a biomimetic precedent for the steps in dioxygen activation by sMMO, from diiron(II) precursor to diiron(IV) oxidant.

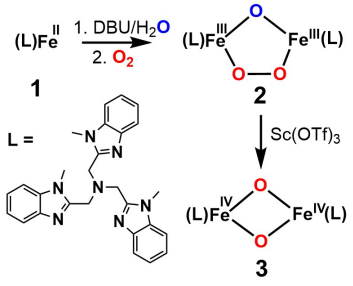

Scheme 1. Reaction of O_2 with **1** in the presence of DBU and water to form **2** and its subsequent conversion to **3**.

Results and Discussion

A colorless 1 mM solution of **1** prepared in CH_3CN under N_2 at -40 °C turns yellow upon addition of 1.5 equiv. DBU/H_2O, corresponding to the appearance of a broad absorption band around 390 nm (Figure 1, left panel). Such spectral changes have been observed when related $Fe^{II}(N4)$ complexes are treated with Et_3N to form dihydroxo-bridged diiron(II) complexes.[29,30] Oxygenation of the [**1** + **DBU**] solution produces a deep-green species **2** with absorption bands at 485, 595 and 750 nm (ε ~ 1200, 1000, 300 M^{-1} cm^{-1}, respectively), features like those associated with (μ-oxo)(μ-1,2-peroxo)diiron(III) complexes.[29,30] This intermediate exhibits a $t_{1/2}$ of 13 min at -40 °C.

Mössbauer spectroscopy of **2** measured at 4.2 K and zero applied field reveals a single quadrupole doublet with an isomer shift (δ) of 0.49 mm/s and a quadrupole splitting (ΔE_Q) of 1.06 mm/s (Figure 1, right panel, top), representing the two equivalent high-spin iron(III) sites of the (μ-oxo)(μ-1,2-peroxo)diiron(III) complex. Notably, the quadrupole splitting of **2** is among the smallest of the values previously reported for peroxodiiron(III) complexes (Table 1).[2] High-field measurements show that the doublet originates from a diamagnetic species that corresponds to 75-80% of the iron in the sample (Figure S1).

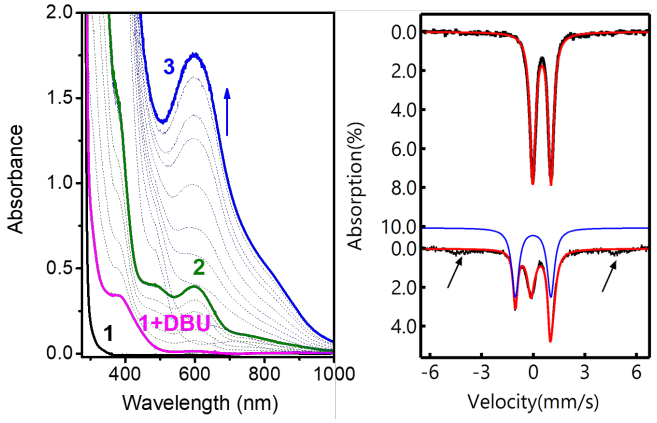

Figure 1. Left panel: UV-vis absorption spectra of **1** (1 mM, black), [**1** + **DBU**] (magenta) formed after addition of 1.5 eq DBU, **2** (green) obtained upon oxygenation of **1** in the presence of DBU, and **3** (blue) formed upon addition of 2 eq $Sc(OTf)_3$ to **2**, all in CH_3CN at -40 °C. **Right panel:** Mössbauer spectra of **2** (top) and **3** (bottom) at 4.2 K and 0 T. The arrows point out features from mononuclear iron(III) impurities. The red traces show the overall simulations of the zero-field spectra, and the blue trace shows the simulation of the diiron(IV) component alone.

The resonance Raman spectrum of **2** obtained with 561-nm excitation of a frozen solution at 77 K shows resonantly enhanced bands at 825, 715, 527, 518 and 454 cm^{-1} (Figure 2, top panel). With $^{18}O_2$, the 825-cm^{-1} band downshifts by 46 cm^{-1}, as predicted by Hooke's law for an O–O stretch. This value is among the smallest ν(O–O)'s found for peroxodiiron(III) complexes (Table 1). Two other vibrations at 454 and 518 cm^{-1} also downshift by about 24 cm^{-1} upon $^{18}O_2$ incorporation, leading to their respective assignments as the ν_{sym}(Fe–O_2–Fe) and the ν_{asym}(Fe–O_2–Fe) modes. On the other hand, the features at 527 and 715 cm^{-1} are sensitive to $H_2{}^{18}O$ labeling, respectively downshifting by 25 and 34 cm^{-1} (Figure 2, top panel), supporting their assignments as the ν_{sym} and ν_{asym} modes of the Fe–O–Fe unit. Taken together, these results strongly suggest that this deep green intermediate is an $Fe^{III}{}_2$(μ-O)(μ-1,2-O_2) complex based on their spectroscopic resemblance to the previously reported complexes with $Fe^{III}{}_2$(μ-O)(μ-1,2-O_2) cores.[2]

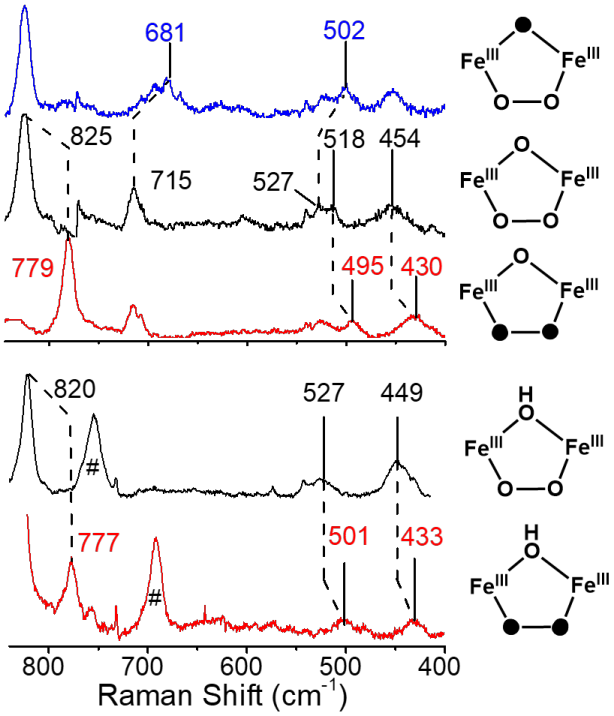

Figure 2. Top panel: Solvent-subtracted resonance Raman spectra of a frozen solution of **2** generated with $^{16}O_2$ in CH_3CN (black), with $^{16}O_2$ in the presence of 150 equiv. $H_2{}^{18}O$ (blue) and with $^{18}O_2$ in CD_3CN (red) at 77 K. **Bottom panel:** Resonance Raman spectra of **2**+H^+ derived from $^{16}O_2$ in CH_3CN (black) and $^{18}O_2$ in CD_3CN at 233 K. (red). Dotted lines connect spectral features that exhibit isotope shifts and # signs denote solvent features. Isotopic composition for different spectra are shown on the right hand side of the figure. Filled oxygen atoms denote ^{18}O-labeled atoms.

Previous studies of synthetic (μ-oxo)diiron(III) and (μ-1,2-peroxo)diiron(III) complexes have uncovered patterns that correlate vibrational frequencies with structural features of these complexes. Sanders-Loehr and co-workers have found that the ν_{sym}(Fe–O–Fe) and ν_{asym}(Fe–O–Fe) values can be correlated with the Fe–O–Fe angle of the complex (Figure 3, top panel),[31] while Fiedler *et al.* have shown a linear relationship between the ν(O–O) of a complex and its diiron distance (Figure 3, bottom panel).[32] When analyzed within this context, the vibrational data of **2** predict an Fe–O–Fe angle of 117° and an Fe•••Fe distance of 3.04 Å for **2**.

Table 1: Comparison of properties of (μ-1,2-peroxo)-diiron(III) complexes

Complex[a] [$t_{1/2}$] @ -40 °C	λ_{max} (ε), nm ($M^{-1}cm^{-1}$)	ν(O–O) (cm^{-1}) [$\Delta^{18}O_2$]	d(Fe•••Fe) (Å)[b]	$\delta[\Delta E_Q]$ (mm/s)	Ref.
μ-oxo complexes					
2 [13 min]	595 (1000)	825 [-46]	3.07	0.49 [1.06]	This work
A BPPE (μ-O_2CCH_3) [8 h/27 °C]	595 (1400)	816 [-45] 830	3.04	0.53 [1.67]	33 32
B BQPA	620 (1000)	844 [-44]	3.13	–	32
C 6Me$_3$TPA [7.5 min/ -30 °C]	648 (1200)	847 [-44]	3.14	0.54 [1.68]	32,34
D 6Me$_2$BPP	577 (1500)	847 [-33]	***3.171***	0.50 [1.46]	35
E 6MeBQPA	640 (1300)	853 [-45]	3.15	–	32
F BnBQA [6 h]	650 (1300)	854 [-47]	3.16	0.55 [1.43]	30
μ-hydroxo complexes					
2+H^+ [75 min]	640 (1300)	820 [-43]	3.09	0.56 [1.17][c]	This ork
G BnBQA [40 min]	730 (2400)	928 [-53]	3.46	0.57 [1.35] 0.56 [0.96]	30
H 6Me$_2$BPP	644 (3000)	908 [-47]	***3.395***	0.50 [1.31]	35

[a] Please refer to Scheme 2 below for the ligand structures and the abbreviations. [b] Distances in bold and italic font are derived from XRD. [c] Represents 70% of the **2**+H^+ sample. The remaining 30% is another quadrupole doublet with δ = 0.45 mm s^{-1} and ΔE_Q = 0.69 mm s^{-1}; its low-field Mössbauer spectrum is shown in Figure S2.

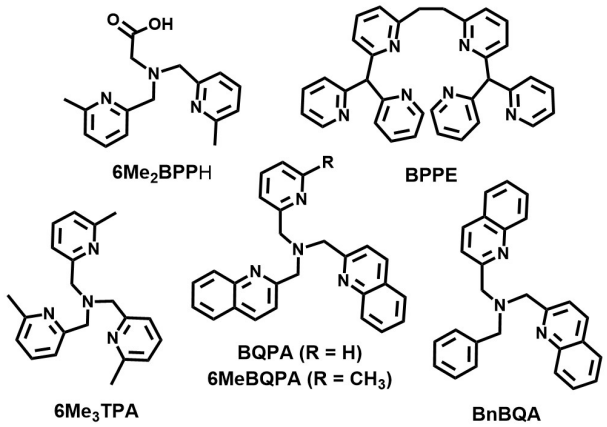

Scheme 2. Ligand structures used in Table 1.

The conclusions derived from the Raman-based correlations have been confirmed by X-ray absorption spectroscopy. The XANES spectrum of **2** has an Fe K-edge energy (E_0) of 7126.3 eV (Figure S6a), consistent with values for high-spin iron(III) centers. The pre-edge region of **2** can be fit with one peak centered at 7114.5 eV with an area of 18.2 units (Figure S6b and Table S2), values comparable with those reported for other complexes with Fe^{III}_2(μ-O)(μ-1,2-O_2) cores.[30,32] The best fit of the EXAFS data obtained for **2** (Figure 4) consists of 2 N/O scatterers at 1.84 Å, 4 N/O scatterers at 2.11 Å, and a diiron distance of 3.07 Å. The two O scatterers with an average Fe–O distance of 1.84 Å would then be assigned to the oxo bridge (average Fe–O distance of 1.81 Å[30,32,34,35]) and the 1,2-peroxo bridge (average Fe–O distance of 1.87 Å[30,32,34,35]).

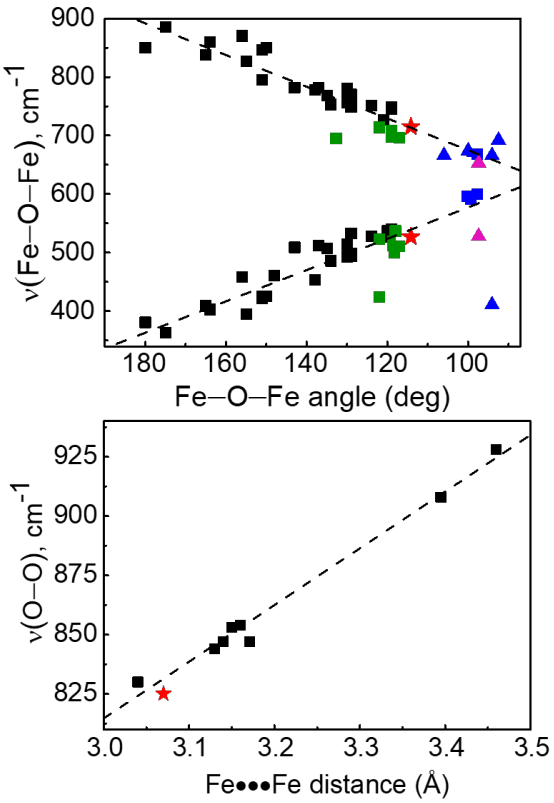

Figure 3. Top panel: Correlation between ν_{sym}(Fe–O–Fe) (bottom) and ν_{asym}(Fe–O–Fe) values (top) of oxo-bridged diiron complexes with their Fe–O–Fe angles. Data from the original Sanders-Loehr study (black)[31] are augmented by data for species with Fe_2(μ-O)(μ-1,2-O_2) (green)[29,30,32,34,35] and Fe_2(μ-O)(μ-OH) cores (blue squares).[36] Additionally, vibrations associated with Fe_2(μ-O)$_2$ diamond cores[37–41] are plotted as blue triangles. For emphasis, the Fe–O–Fe vibrations of **2** are shown as red stars, while those for **3** are indicated by pink triangles. The black dashed lines show the best linear fit of the data points available. **Bottom panel:** Plot of Fe•••Fe distance vs. ν(O–O) frequencies available for model peroxodiiron(III) complexes having an additional oxo or hydroxo bridge.[30,32] **2** is represented as a red star.

Of particular interest is the fact that the diiron distance of **2** is among the shortest of the peroxodiiron(III) model

complexes reported so far (Table 1). This observation is tied to the fact that **2** has one of the lowest observed ν(O–O)'s among such complexes (Figure 3, bottom panel). Furthermore, the 113° Fe–O–Fe angle obtained from the EXAFS data agrees well with that derived from the Sanders-Loehr correlation relating the Fe–O–Fe vibrations with the Fe–O–Fe angle (Figure 3, top panel, red stars).

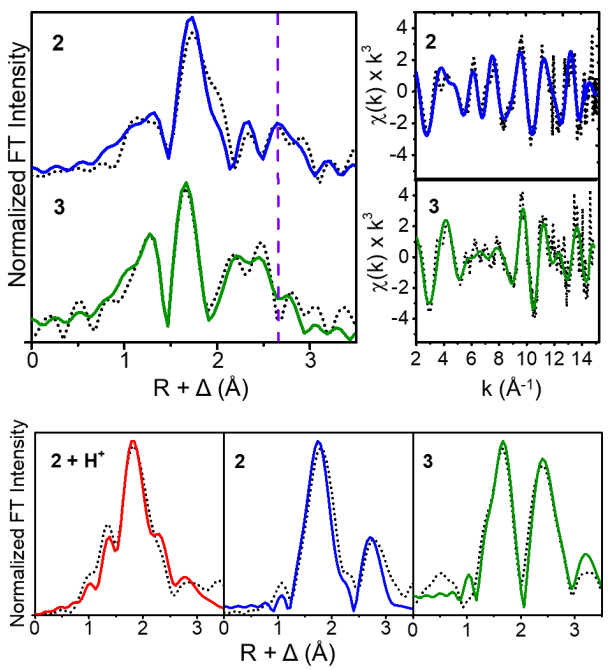

Figure 4. Top left panel: Fourier-transformed *k*-space EXAFS data for **2** (top) and **3** (bottom). The vertical dashed purple line highlights the feature associated with the Fe scatterer in **2**, and its change between **2** and **3**. **Top right panel:** *k*-space EXAFS data (k^3-multiplied) for **2** (top) and **3** (bottom). Data is represented by black dots, and best fits are blue for **2** and green for **3**. **Bottom panel:** k^5-multiplied EXAFS data for **2**+**H**$^+$, **2**, and **3**.

A comparison of the spectroscopic properties of the (μ-oxo)(μ-1,2-peroxo)diiron(III) complexes listed in Table 1 shows that **2** has properties that most closely resemble those of **A**, $[Fe^{III}_2(\mu\text{-O})(\mu\text{-1,2-O}_2)(OAc)(BPPE)]^+$, where BPPE provides 6 pyridines to support a $[Fe^{III}_2(\mu\text{-O})(\mu\text{-1,2-O}_2)(\mu\text{-OAc})$ core. Complexes **2** and **A** are distinct from the others on the list in having blue-shifted peroxo(π_v*)-to-iron(III) (d_π orbital) charge transfer bands in the visible region, lower ν(O–O) values, and shorter Fe•••Fe distances. Complex **2** is the only complex on the list with benzimidazole donors, which are more basic than the pyridine and quinoline donors found on the other complexes[42] and thus expected to decrease the Lewis acidity of the iron(III) centers in **2** and give rise to the blue shift of its absorption maximum. In the case of **A**, the addition of a carboxylate bridge serves to lower the Lewis acidity of the metal centers. More importantly, these two complexes resemble each other in having the lowest ν(O–O) values and the shortest diiron distances in the series (Table 1). For **A**, the bridging acetate and the ethylene linker of the dinucleating ligand bring the two iron atoms closer to each other and presumably give rise to the lower ν(O–O) observed, but it is quite remarkable that **2** has the same features without similar structural constraints.

The lower ν(O–O) of **2** suggests that its O–O bond may be weaker than those of the other reported (μ-oxo)(μ-1,2-peroxo)diiron(III) complexes (Table 1). Additionally, the half-life of **2** (13 min at -40 °C) is also quite short when compared with related complexes in Table 1. The weakened bond and short half-life might prime it to undergo O–O bond cleavage by addition of a suitable acid and convert **2** into a high-valent diiron species.[30,32] However, addition of 1.5 eq $HClO_4$ (or HOTf) red-shifts its λ_{max} from 595 nm to a broader feature of comparable intensity around 640 nm (ε = 1300 M^{-1} cm^{-1}) (Figures S10 and S11). This change is accompanied by the loss of the Raman features associated with the Fe–O–Fe unit (Figure 2, bottom panel) while retaining those of the Fe–O–O–Fe unit, suggesting the protonation of the oxo bridge of **2** to its μ-hydroxo derivative **2**+**H**$^+$. This change is corroborated by EXAFS analysis of **2**+**H**$^+$ (Figure S7) showing the lengthening of the average Fe–O bond distance from 1.84 to 1.89 Å, an increase that is also observed upon protonation of the oxo bridge of $[Fe^{III}_2(\mu\text{-O})(\mu\text{-1,2-O}_2)(BnBQA)_2]^{2+}$.[30]

Surprisingly, the Fe•••Fe distance of **2**+**H**$^+$ is essentially unchanged within experimental error from that of **2** (3.09 vs 3.07 Å, respectively) and shorter than the ~3.4-Å distances found for the other two (μ-hydroxo)(μ-1,2-peroxo)-diiron(III) complexes characterized to date (**G** and **H** in Table 1). The comparable Fe•••Fe distances of **2** and **2**+**H**$^+$ are corroborated by the similar ν(O–O) values found for **2** and **2**+**H**$^+$, based on the correlation in Figure 3, bottom panel, and can be contrasted with the much higher ν(O–O) values of >900 cm^{-1} associated with **G** and **H**. Lastly, **2** in fact becomes more stable upon protonation at -40 °C, increasing in half-life nearly 6-fold from 13 min to 75 min (Figure S9), while $[Fe^{III}_2(\mu\text{-O})(\mu\text{-1,2-O}_2)(BnBQA)_2]^{2+}$ decreases in half-life by 10-fold (Table 1). Thus protonation affects the stabilities of the Me_3NTB and BnBQA peroxo complexes in opposite directions for reasons we do not yet fully understand.

In stark contrast, treatment of **2** with the Lewis acid $Sc(OTf)_3$ in place of strong acid results in the cleavage of its O–O bond to afford a diiron(IV) complex **3**. This outcome is manifested by the growth of an intense absorption feature at 600 nm (9000 M^{-1} cm^{-1}) that forms over the course of an hour at -40 °C (Figure 1). Excitation of the intense visible chromophore of **3** using a 660-nm laser at -40 °C elicits resonantly enhanced Raman bands at 653 and 528 cm^{-1}, which downshift respectively by 30 and 17 cm^{-1} in a sample of $^{18}O_2$-labeled **3** (Figure 5). The vibrational frequency of 653 cm^{-1} with an isotopic shift of 30 cm^{-1} for **3** reflects an Fe–O–Fe angle of close to 100°, characteristic of complexes with an $M_2(\mu\text{-O})_2$ 'diamond core'.[37–41,43] Such an acute angle has thus far only been shown to be enforced by the presence of a second μ-oxo bridge. Furthermore, experiments starting with a 1:1 mixture of $^{16}O_2$-labeled **2** and $^{18}O_2$-labeled **2** to form **3** show the formation of $Fe^{IV}_2(\mu\text{-O})_2$

species having either two ^{16}O atoms or two ^{18}O atoms but with no evidence for a mixed-$^{16}O^{18}O$ complex, which should exhibit an intermediate frequency of 638 cm^{-1} (Figure S8). Thus, both oxygen atoms in **3** must derive from the peroxo moiety of one unique molecule of **2** (Figure S8) and the oxo-bridged O-atom in **2** must be released from the complex, presumably upon combination with $Sc(OTf)_3$.

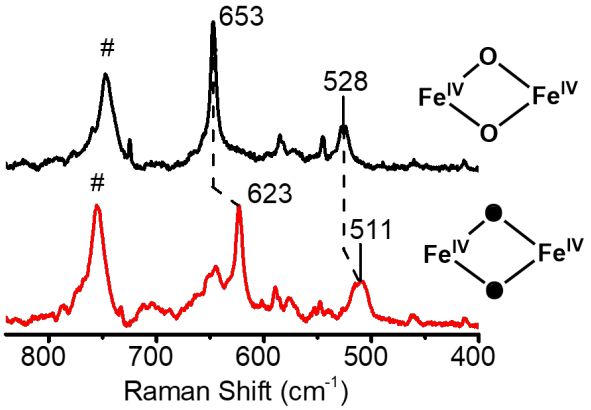

Figure 5: Resonance Raman spectra of **3** in CH_3CN derived from $^{16}O_2$ (black) and $^{18}O_2$ (red). The latter was prepared from ^{18}O-labeled **2** generated from the reaction of [**1** + **DBU**] with $^{18}O_2$. Dotted lines highlight observed isotope shifts, while # signs correspond to solvent features. Filled oxygen atoms denote ^{18}O isotope incorporation into **3.**

Table 2: Properties of $Fe_2(\mu\text{-}O)_2L_2$ complexes

Complex	ν(Fe–O) [$\Delta^{18}O$] (cm^{-1})	∠Fe–O–Fe (°)	d(Fe••Fe) (Å)	Ref.
3	653 [-30] 528 [-17]	97	2.70	This work
M = Fe^{IV} L = TPA*	674 [-30]	101 [a]	2.73	39
M = Fe^{III} L = 6-Me_3TPA	692 [-32]	***92.5*** [b]	***2.714*** [b]	40,41
M = $Fe^{3.5}$ L = 5-Et_3-TPA	666 [-35] 411 [-15]	***94.1*** [b]	***2.683*** [b]	37,38
M = $Fe^{3.5}$ L = R_3-TPA R = H, 3-Me, or 5-Me	666-668 [-(28 -32)] 404-411 [-(13 -16)]			41
sMMO-**Q**	690 [-36]		~3.4	19,44

[a] Calculated based on r_{Fe-O} and $r_{Fe\cdots Fe}$ values obtained from EXAFS data. [b] Values obtained by X-ray crystallography. See Scheme 3 below for ligand structures and acronyms.

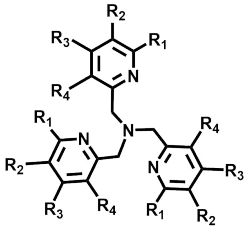

$R_1 = R_2 = R_3 = R_4 = H$	TPA
$R_1 = Me, R_2 = R_3 = R_4 = H$	6-Me_3TPA
$R_2 = Me, R_1 = R_3 = R_4 = H$	5-Me_3TPA
$R_2 = Et, R_1 = R_3 = R_4 = H$	5-Et_3TPA
$R_1 = R_2 = R_3 = H, R_4 = Me$	3-Me_3TPA
$R_1 = H, R_2 = R_4 = Me, R_3 = OMe$	TPA*

Scheme 3. Structures of ligands used in Table 2.

The 653-cm^{-1} Raman band is reminiscent of the 674 cm^{-1} feature reported for $[Fe^{IV}_2(\mu\text{-}O)_2(TPA^*)_2]^{4+}$,[39] which is associated with an A_1 breathing mode of an $Fe_2(\mu\text{-}O)_2$ core that has an Fe–O–Fe angle of 100°.[38,41] Furthermore, the observation of an ^{18}O-isotope shift of ~30 cm^{-1} confirms that this vibration is essentially an Fe–O stretching mode. Interestingly, the 653-cm^{-1} peak falls within error on the higher frequency line in Figure 3 (top panel), which represents the asymmetric Fe–O–Fe modes of the Fe–O–Fe complexes. The corresponding features for $[Fe^{IV}_2(\mu\text{-}O)_2(TPA^*)_2]^{4+}$, $[Fe^{II}Fe^{IV}(\mu\text{-}O)_2(R\text{-}TPA)_2]^{3+}$, and $[Fe^{III}_2(\mu\text{-}O)_2(6\text{-}Me_3\text{-}TPA^*)_2]^{2+}$, shown as triangles, also fall on this line (see Table 2 for a comparison of properties for $Fe_2(\mu\text{-}O)_2$ complexes). A similar assignment for the 650-700-cm^{-1} vibration observed in $[Fe^{III}Fe^{IV}(\mu\text{-}O)_2(R\text{-}TPA)_2]^{3+}$ complexes has been made by Solomon and co-workers using normal coordinate analysis.[38]

Complex **3** also exhibits a peak at 528 cm^{-1} with an ^{18}O-isotope shift of 17 cm^{-1}, which would arise from a different Fe_2O_2 mode. Such a feature has thus far not been observed for any other complex with an $Fe_2(\mu\text{-}O)_2$ core, but all the valence-delocalized $[Fe^{III}Fe^{IV}(\mu\text{-}O)_2(R_3\text{-}TPA)_2]^{3+}$ complexes show a feature near 410 cm^{-1} with comparable ^{18}O-isotope shifts,[41] suggesting that these modes may be related, a notion corroborated by our computational studies (*vide infra*). Clearly, these features do not fall on the lower frequency line of the correlation shown in Figure 2 top panel that represents the symmetric Fe–O–Fe modes of the Fe–O–Fe complexes. However, further studies exploring the connection between Fe–O–Fe complexes that have effective C_{2v} symmetry and the diamond core complexes that have effective C_{2h} symmetry are worth pursuing.

The Mössbauer spectrum of ^{57}Fe-enriched **3** obtained in zero applied field at 4.2 K exhibits two quadrupole doublets (Figure 1, right panel). One doublet has an isomer shift (δ) of -0.04 mm s^{-1} and a quadrupole splitting (ΔE_Q) of 2.00 mm s^{-1}, values nearly identical to those of $[Fe^{IV}_2(O)_2(TPA^*)_2]^{4+}$ (δ = -0.04 mm s^{-1} and ΔE_Q = 2.09 mm s^{-1}).[39] The diiron(IV) state in **3** is validated by field-dependent studies performed at 4.2 K with various applied magnetic fields (2.0 T, 4.0 T, 7.0 T) (Figure S3). The other doublet has δ = 0.48 mm s^{-1} and ΔE_Q = -1.22 mm s^{-1}, parameters typical of a high-spin diferric species that likely derives from **3** decay. A third component corresponds to a mononuclear high-spin Fe(III) byproduct that is most easily identified in the high-field spectra. After the high-spin ferric component is subtracted out, a cleaner spectrum with only diiron(III) and diiron(IV) components can be

obtained (Figure S4). Analysis of all the spectra from two different samples of ^{57}Fe-enriched **3** shows that the samples contain ~35% of the diiron(IV) complex, together with 35% of a diferric species and 25% of high-spin ferric components (see Table S1 for more details).

XAS studies also support the assignment of **3** as having an $Fe^{IV}_2(\mu\text{-}O)_2$ core. The XANES region in Figure S6a shows an increase in the K-edge energy of more than one eV from 7126.3 eV for **2** to 7127.5 eV for **3** (Figure S6b and Table S2), consistent with an increase in the average iron oxidation state in the latter sample. The K-edge energy value for **3** is not as high as that for $[Fe^{IV}_2(\mu\text{-}O)_2(TPA^*)_2]^{4+}$ (7130.1 eV), due to the smaller fraction of **3** (~40%) present in these samples than found in preparations of $[Fe^{IV}_2(\mu\text{-}O)_2(TPA^*)_2]^{4+}$ (86-90%).[39] (The XAS sample of **3** was prepared from its ^{56}Fe precursor, which afforded a slightly higher yield of **3** than the ^{57}Fe-labeled precursor used to prepare the Mössbauer sample.)

EXAFS analysis also provides strong support for having a component with an $Fe^{IV}_2(\mu\text{-}O)_2$ diamond core in the XAS sample of **3**. The primary coordination sphere consists of N/O scatterers at 1.78, 1.95, and 2.09 Å (compared to 2 N/O scatterers at 1.84 Å and 4 N/O scatterers at 2.11 Å for **2**). The contraction of average bond lengths for first shell scatterers is consistent with the oxidation of some of the iron centers. More tellingly, one component has a significantly shortened Fe•••Fe distance of 2.70 Å, which is almost identical to that found for $[Fe^{IV}_2(\mu\text{-}O)_2(TPA^*)_2]^{4+}$ (Tables 2 and 3). The n value for this Fe scatterer has been constrained to 0.4 to reflect the fraction of **3** in the XAS sample, leading to a very small Debye-Waller factor (Table S3) similar to that found for $[Fe^{IV}_2(\mu\text{-}O)_2(TPA^*)_2]^{4+}$,[39] which reflects the rigidity of the diamond core motif. From the EXAFS fit of **3**, an Fe–O–Fe angle of 97° can be calculated. As a further test of our EXAFS analysis approach, the $\chi(k)$ data were multiplied by k^5 in order to magnify the contributions of heavier-atom scatterers.[45] These contributions become particularly apparent in the Fourier-transformed data (Figure 4, bottom panel), where features in the second coordination sphere increase in intensity in the order of **2**+H^+, **2** and **3**, with the shortening of the Fe•••Fe distance and the increased rigidity of the diiron unit.

Table 3: Comparison of EXAFS-derived iron-scatterer distances for **2** and **3** and related complexes

Complex [a]	d(Fe–O) (Å)	d(Fe–N) (Å)	d(Fe••Fe) (Å)	Ref.
$Fe^{III}_2(\mu\text{-}O)(\mu\text{-}1,2\text{-}O_2)$ complexes				
2	2 @ 1.84	4 @ 2.11	3.07	This work
2+H^+	2 @ 1.89	4 @ 2.09	3.09	
A BPPE (μ-O_2CCH_3)	1 @ 1.77 2 @ 1.94	3 @ 2.16	3.04	[32]
B BQPA	2 @ 1.82	1 @ 2.03 3 @ 2.21	3.13	[32]
C 6Me$_3$TPA	2 @ 1.84	4 @ 2.23	3.14	[32,34]
E 6MeBQPA	2 @ 1.83	1 @ 2.05	3.15	[32]
		3 @ 2.23		
F BnBQA	1 @ 1.81 1 @ 1.92	4 @ 2.21	3.16	[30]
$Fe^{IV}_2(\mu\text{-}O)_2(L)_2$ diamond core complexes				
L = Me$_3$NTB (**3**)	2 @ 1.79	2 @ 1.97 2 @ 2.09	2.70	This work
L = TPA*	2 @ 1.78	4 @ 1.97	2.72	[39]

Similar UV-vis spectral changes are seen when **2** is treated with $Al(OTf)_3$ as the Lewis acid (Figure S13). However, the addition of $Yb(OTf)_3$, $Y(OTf)_3$, $Zn(OTf)_2$, $Ca(OTf)_2$, or $Ba(OTf)_2$ does not result in the formation of **3**, suggesting that the other Lewis acids are not powerful enough to convert **2** into **3**.[46,47,48] Similar effects of changing the strength of the added Lewis acid have been observed for the cleavage of the O–O bond of $[(TMC)Fe^{III}(\eta^2\text{-}O_2)]^+$ by Sc^{3+} and Y^{3+} ions.[49,50,51] In the latter study, both ions promote O–O bond cleavage to form the $[(TMC)Fe^{IV}(O)]^{2+}$ derivative but at rates that depend on the Lewis acidity of the metal ions. Interestingly, the Lewis acid effect of Sc^{3+} on **2** can be nullified by the presence of 200 mM water (Figure S14), and **2**+H^+ is formed instead. This effect resembles the effect of treating **2** with $HClO_4$ or HOTf (Figures S10 and S11) and suggests that $Sc(OTf)_3$ hydrolyzes under these conditions to produce protons in solution to give rise to **2**+H^+.

The temperature dependence for the conversion of **2** to **3** has been investigated to obtain activation parameters. Eyring analysis in the range of 233 to 253 K gives $\Delta H^‡$ = 55(2) kJ mol^{-1} and $\Delta S^‡$ = -62(10) J mol^{-1} K^{-1} (Figure S15), which are compared in Table 4 to those reported for related O–O bond cleavage steps in other iron(III)-peroxo complexes. To date, there are only two other peroxodiiron(III) complexes with such data for comparison. One example is the decay of $[(TMP)Fe^{III}–O–O–Fe^{III}(TMP)]$ into two mononuclear oxoiron(IV) complexes with $\Delta H^‡$ = 61(4) kJ mol^{-1} and $\Delta S^‡$ = -63(4) J mol^{-1} K^{-1},[52] which are quite similar to those for the conversion of **2** to **3**. A second example is the interesting diiron chemistry reported by Kodera for 6-HPA,[53,54] an octadentate dinucleating ligand that supports a (μ-oxo)(μ-1,2-peroxo)diiron(III) center, which undergoes subsequent O–O bond cleavage to generate a putative (μ-oxo)bis(oxoiron(IV)) species. Although Kodera has assigned the obtained Eyring parameters to the *syn*-to-*anti* isomerization of the $[O=Fe^{IV}–O–Fe^{IV}=O]$ moiety, we propose a different interpretation based on the nearly identical activation parameters determined for this step and for the conversion of **2** to **3** and their strong similarity to other entries in Table 4 associated with O–O bond homolysis. We thus conjecture that both **2** and $[(6\text{-}HPA)Fe^{III}_2(\mu\text{-}O)(\mu\text{-}1,2\text{-}O_2)]^{2+}$ undergo rate determining O–O homolysis to generate diiron(IV) species.

Table 4. Eyring activation parameters for peroxoiron(III) decay in MeCN solvent unless otherwise indicated.

Peroxo complex[a]	$\Delta H^{\ddagger}$ kJ mol^{-1}	$\Delta S^{\ddagger}$ J K^{-1} mol^{-1}	O–O cleavage mode proposed	Ref
2 + $Sc(OTf)_3 \rightarrow$ **3**	55(2)	-62(10)	Homo-lysis	a
[(6-HPA)Fe^{III}_2(μ-O)(μ-1,2-O_2)]$^{2+}$	57	-50	Homo-lysis [b]	54
(TMP)Fe^{III}–O–O–Fe^{III}(TMP) in toluene	61(4)	-63(4)	Homo-lysis	52
(N_4Py)Fe^{III}–OOH in acetone/ CF_3CH_2OH	53(1)	-121(2)	Homo-lysis	55
(TPA)Fe^{III}–OO^{t}Bu	52(1)	-74(3)	Homo-lysis	56
(TPA)Fe^{III}(κ^2-$OOC(CH_3)_2OH$) in acetone	54(3)	-35(13)	Homo-lysis	57
(TPA)Fe^{III}–OOH	45(2)	-95(10)	Hetero-lysis	58
(TMC)Fe^{III}–OOH in acetone/ CF_3CH_2OH	56(2)	-75(2)	Homo-lysis	55
(TMC)Fe^{III}–OOH + $HClO_4$	44(2)	-90(10)	Hetero-lysis	59

[a] This work.
[b] See text for our interpretation of the 6-HPA results, which differs from Kodera's.
For ligand abbreviations used in Table 4, see Scheme 4 below.

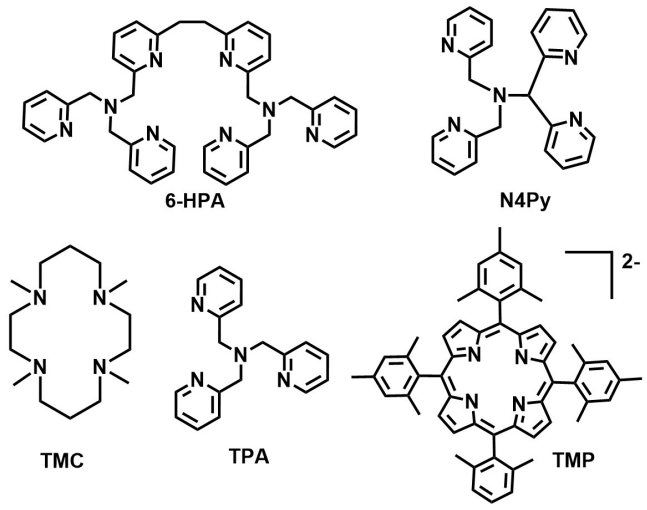

Scheme 4. Ligand structures and acronyms used in Table 4.

A mechanism for the conversion of **2** to **3** is proposed in Scheme 5 that accounts for the incorporation of both peroxo oxygen atoms from a unique molecule of **2** into the product **3** (Figure S8). Intermediate **2** has been shown to have a Fe^{III}_2(μ-O)(μ-1,2-O_2) core by an array of spectroscopic techniques. The fact that the peroxo oxygen atoms in **2** are completely retained in the resultant Fe^{IV}_2(μ-O)$_2$ core of **3** requires the water-derived oxo bridge of **2** to be lost prior to the formation of **3**, a disposal function that presumably can be assigned to the highly Lewis acidic Sc^{3+} (or Al^{3+}) ion. Upon loss of the oxo bridge in **2**, both iron coordination spheres become coordinately unsaturated and the peroxo O-atoms remaining on the μ-oxo-depleted **2** are then poised to isomerize from μ-1,2 binding to a μ-η^2:η^2 coordination mode that would set the stage for the subsequent O–O bond cleavage step to generate the bis(μ-oxo)diiron(IV) product **3**. Similar conversions have been well established in dicopper model systems since 1996.[60,61] Treatment with Sc^{3+} (or Al^{3+}) is found to promote O–O bond cleavage in **2**, which is likely to occur homolytically based on the similarity of the activation parameters for the generation of **3** to those of other O–O cleaving reactions (Table 4). Further insight into the mechanism is provided by DFT calculations presented in the next section.

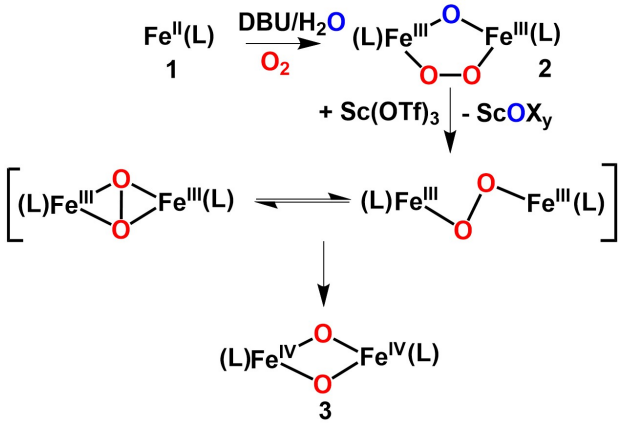

Scheme 5. Proposed mechanism for the conversion of **2** to **3**. The water-derived O-atom shown in blue is lost during the course of the reaction, possibly by binding to Sc^{3+}.

Insight into how Sc^{3+} may promote the conversion of **2** to **3** has been obtained from DFT calculations at the S12g/TZ2P level of theory.[62,63] For this we need to show the computed structures of **2** and **3**, and be certain that these are indeed responsible for the measured (vide supra) spectroscopic fingerprints. The optimized structure of **2** (Figure 6) shows antiferromagnetic coupling of the high-spin iron(III) atoms, leading to an Fe•••Fe distance of 3.09 Å (in excellent agreement with the EXAFS-derived value of 3.07 Å for **2** (Table 1) and an Fe–O–Fe angle of 118°. In this structure, the Me_3NTB ligands adopt a configuration designated as DU, in which one ligand point downwards with the peroxo moiety below the oxo bridge, and the other upwards. Studies of other configurations, namely down-down (DD) and up-up (UU), as well as ferromagnetically (FM) vs. antiferromagnetically (AFM) coupled iron centers for all three ligand configurations, find the AFM-DU isomer to be the most stable (with DD only slightly less stable by ca. 1 kcal·mol^{-1}, and UU and ferromagnetically coupled isomers less stable by 10-15 kcal·mol^{-1}).

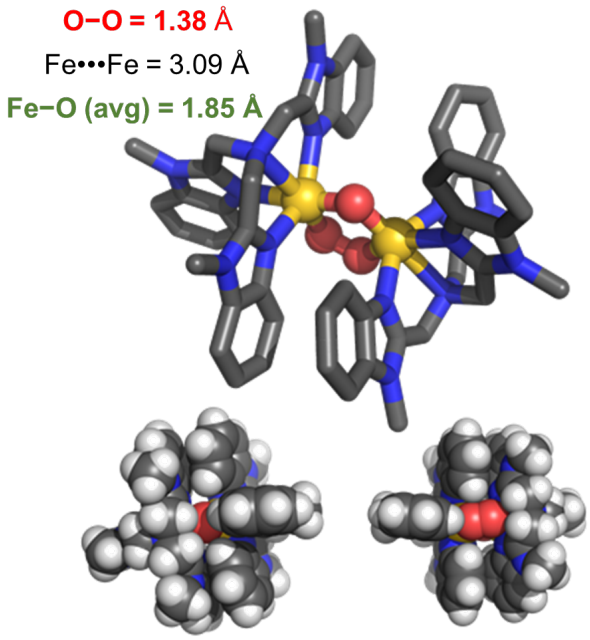

Figure 6. Top panel: S12g/TZ2P optimized structure for **2** in the DU configuration **Bottom panel:** Spacefill diagrams of **2**, showing the accessibility of the oxo and the peroxo sides of the molecule.

These DFT results are supported by the crystal structures of **D** and **H** (Table 1), both of which exhibit DU ligand conformations. We have thus investigated all the complexes in Table 1 by DFT and found that most of them (**B** - **H**) have a preference for the DU conformer. The structure of **A** is an exception as it cannot be classified as DD or DU due to constraints imposed by the ethylene tether between the two halves of the octadentate ligand. Interestingly, Figure S17 shows a good correlation between the computed O–O stretching frequencies and the experimentally observed values (R^2 = 0.94). Most of computed frequencies are somewhat overestimated, just like the O–O vibration in H_2O_2, which is calculated to be 923 cm^{-1} versus an experimental value of 872 cm^{-1}. On the other hand, the low value for the O–O vibration of 825 cm^{-1} in **2** is also predicted well by DFT (after scaling according to the linear fit from Fig. S17), with a value of 841 cm^{-1}. This good correlation between observed and calculated results stems directly from the use of the S12g functional, which is able to give a good description of electronic structures for antiferromagnetically coupled high-spin diiron(III) species, unlike other functionals like BP86-D3. The correlation from Figure S17 may also be useful for future experimental studies, when experimental determination of vibrational frequencies proves to be difficult. The computed Mössbauer parameters for **2-DU** (δ = 0.45-0.47 mm/s, ΔE_Q = 0.80-0.95 mm/s) are in good agreement with the experimental values (δ = 0.49 mm/s, ΔE_Q = 1.06 mm/s) found for **2**.

For diiron(IV) species **3-DU** isomer, DFT calculations predict Fe–N distances of 1.96-1.97 Å for the benzimidazole donors and 2.13 Å for the amines, an Fe•••Fe distance of 2.70 Å and Fe–O–Fe angles of 98°, in very good agreement with the EXAFS analysis. The **3-DD** form is less stable than **3-DU** by 16.1 kcal/mol, which is consistent with the structures of related crystallographically characterized Fe_2O_2 diamond-core complexes reported so far.[36,37,40,64] As it is difficult to visualize how **2-DD** could easily transform into **3-DU**, we have assumed that both **2** and **3** are in fact in the **DU** form.

Surprisingly, the Fe•••Fe distances in the simpler models for **2**, $[Fe^{III}_2(\mu\text{-}O)(\mu\text{-}O_2)(NH_3)_8]^{2+}$ (**m2**, 3.12 Å), and **3**, $[Fe^{IV}_2((\mu\text{-}O)_2(NH_3)_8]^{4+}$ (**m3**, 2.69 Å), remain close to the values experimentally found for **2** and **3**, suggesting that these features are intrinsic characteristics of the two diiron cores and not significantly affected by the nature of the supporting Me_3NTB ligand. The computed Mössbauer parameters for **3** (δ = -0.046 $mm{\cdot}s^{-1}$, ΔE_Q = 2.12 $mm{\cdot}s^{-1}$) and vibrational frequencies (see Figure 7 and Table S5) are consistent with experiment. The 664 cm^{-1} peak can be assigned to ν_3, the fully symmetric breathing mode, while the 531 cm^{-1} peak can be assigned to ν_2, the antisymmetric stretching vibration. This latter vibration likely corresponds to the 448-cm^{-1} frequency calculated for the valence-delocalized ferromagnetically coupled Fe(III)/Fe(IV) analogue of **m3**, which is in agreement with the assignment made by Solomon and co-workers[38] for the ~400-cm^{-1} feature found in the resonance Raman spectra of $[Fe^{III}Fe^{IV}(\mu\text{-}O)_2(R_3\text{-}TPA)_2]^{3+}$ complexes.[41] The normal mode corresponding to ν_3 consists almost entirely of movements of the oxygen atoms (87%), while those in ν_2 are reduced to ca. 55%, which rationalizes the larger ^{18}O-isotope effects found for the 664 cm^{-1} diamond core vibration.

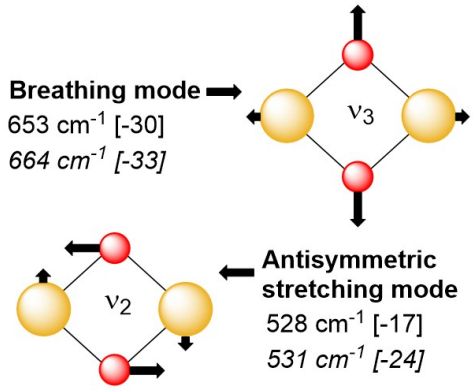

Figure 7. Atomic displacement vectors for the centrosymmetric normal modes calculated for **3** with experimentally observed (normal text) and predicted (italics) frequencies and ^{18}O-isotope shifts in square brackets listed below each mode. See Fig S20 and Table S5 in SI for information on all 6 M_2O_2 modes.

With confidence that the computed structures are responsible for the experimental spectra, we can return to the question of what effect the Lewis acids exert. Adding $Sc(OTf)_3$ to **2** leads to its coordination to the peroxo moiety, which is favored by ca. 47 $kcal{\cdot}mol^{-1}$ over the binding to the oxo bridge (see Figure S18). Scrutiny of this calculated structure shows greater accessibility of the peroxo oxygens than the oxo bridge, which is shielded by the Me_3NTB ligands (see Figure 6 bottom and Figure 8). It is

thus plausible that the preference of Sc^{3+} for peroxo attack derives from steric interactions. Even though the Me_3NTB ligands do shield the oxo side quite well, the preference for Sc^{3+} binding to the peroxo bridge persists even for the simpler model with ammonia ligands (see Figure S18), where no such steric interactions are present. Indeed $Sc(OTf)_3$ binding to the peroxo unit is favored over the oxo bridge by 12 kcal·mol^{-1} in $[Fe^{III}_2(\mu\text{-}O_2)(\mu\text{-}O)(NH_3)_8{\cdot}Sc(OTf)_3]^{2+}$. Interestingly, the separation of the interaction between $Sc(OTf)_3$ and the diiron species into deformation energy (or strain) and interaction energy (following the Distortion/Interaction-Activation Strain Model[65]) shows that the intrinsic preference for the peroxo side derives only from deformation. In the process of binding $Sc(OTf)_3$ by **m2**, the diiron species needs to adjust itself only slightly on the peroxo side (deformation of 6.9 kcal·mol^{-1}) versus 18.5 kcal·mol^{-1} for the binding to the oxo side, which is 2.5 times larger. For both sides, the interaction energy of the $Sc(OTf)_3$ with the **m2** diiron species is the same (-58.1 kcal·mol^{-1}, see Figure S19). In the real systems, these energies are larger: for **2** to bind $Sc(OTf)_3$ the deformation energy (11.3 kcal·mol^{-1}, see Figure S18) is somewhat larger than that of the model system, but this increase by 4.4 kcal·mol^{-1} is compensated for largely by an increase of the interaction energy of 4.5 kcal·mol^{-1}, leading overall to almost similar total binding energies for $Sc(OTf)_3$ (ca. -51 kcal·mol^{-1}).

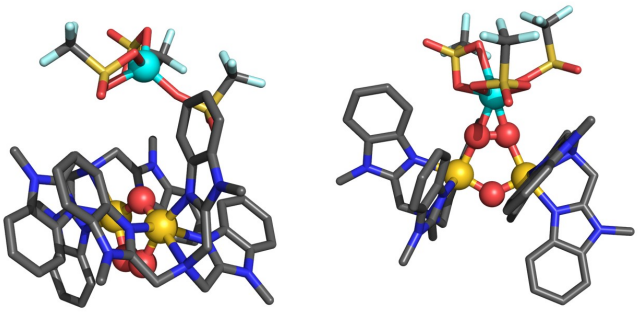

Figure 8. DFT-calculated structures of $Sc(OTf)_3$ adducts to **2** with the Sc placed on the oxo side (left) or on the peroxo side (right).

Lastly, the identification of a second example of a tetradentate tripodal N4 ligand able to support bis(μ-oxo)diiron(IV) core opens the door for comparing the C–H bond oxidative power of **3** relative to that of $[Fe^{IV}_2(\mu\text{-}O)_2(TPA^*)_2]^{4+}$ as well as their mononuclear $[Fe^{IV}(O)(N4)]^{2+}$ counterparts. This question has been explored with 1,4-cyclohexadiene (CHD; BDE = 78 kcal mol^{-1}) as substrate. At 233 K CHD addition to a solution of **3** in CH_3CN results in the first order decay of its 600-nm chromophore and a second order rate constant (k_2) of 7 * 10^{-4} M^{-1}s^{-1} (Figure S16). This value is comparable to the k_2 value of 10^{-4} M^{-1} s^{-1} reported for the oxidation of 9,10-dihydroanthracene by $[Fe^{IV}_2(\mu\text{-}O)_2(TPA^*)_2]^{4+}$ at 193 K,[66] after extrapolation to 233 K by assuming that rates double with every 10 K increase in temperature to give a value of 1.6 x 10^{-3}, making the k_2 for **3** at 233 K only a factor of 2 smaller than that for $[Fe^{IV}_2(\mu\text{-}O)_2(TPA^*)_2]^{4+}$.

In contrast, the corresponding mononuclear complex $[Fe^{IV}(O)(Me_3NTB)]^{2+}$ is one of the most reactive nonheme $Fe^{IV}(O)$ complexes described to date, with k_2 = 9.4 * 10^2 M^{-1}s^{-1} for 1,4-CHD oxidation in CH_3CN at 233 K,[28] nearly 10^7-fold more reactive towards 1,4-CHD than **3**. This result suggests that a terminal oxo is more reactive towards C–H bonds than a bridging oxo if other variables such as oxidation states and spin states of the iron center are kept constant.[66] For comparison, the mononuclear $[Fe^{IV}(O)(TPA^*)]^{2+}$ is 1000-fold more reactive than the corresponding dinuclear $[Fe^{IV}_2(\mu\text{-}O)_2(TPA^*)_2]^{4+}$ complex.[66] These complexes represent the only two pairs of iron(IV)-oxo complexes supported by the same ligand framework but differ in having terminal or bridging oxo units. The 10^4-fold greater reactivity difference found for the Me_3NTB pair of complexes is quite amazing, and a phenomenon that deserves further scrutiny.

Lastly, it needs to be emphasized here that **3** and $[Fe^{IV}_2(\mu\text{-}O)_2(TPA^*)_2]^{4+}$ are far less reactive than sMMO intermediate **Q**, where the latter can oxidize the strong and unactivated C–H bonds of methane efficiently at 4 °C. This disparity may stem from differences in the spin states of the iron(IV) centers, S = 1 for both **3** and $[Fe^{IV}_2(\mu\text{-}O)_2(TPA^*)_2]^{4+}$ and S = 2 for the much more reactive **Q.**[66–68] There are also differences in the diiron(IV) core structures deduced from resonance Raman and X-ray absorption spectroscopy that have yet to be resolved.[19,44] Further scrutiny of these structure-reactivity correlations is desirable.

Summary and Perspectives

In summary, **3** represents the first diiron(IV) complex to be generated by Lewis acid-assisted O–O bond cleavage of a peroxodiiron(III) complex that is derived from the reaction of O_2 with a diiron(II) precursor (black/red pathway in Scheme 6). This transformation is closely related to that of the proton-assisted conversion of sMMO-**P** to sMMO-**Q**.[17,18]

The actual structure of the diiron(IV) core for **Q** is currently not settled, where resonance Raman data support a closed-core structure[19] but recent XAS data[44] favor an open-core structure.

Nevertheless, our study is unique in that it involves the conversion of a peroxodiiron(III) complex to a diiron(IV) complex analogous to the diiron center in the sMMO enzyme. In prior related biomimetic examples in the nonheme literature, (μ-1,2-peroxo)diiron(III) intermediates have been trapped and found to convert into higher-valent diiron derivatives upon treatment with Bronsted acids (along the black path in Scheme 6). Specifically, $[Fe^{III}_2(\mu\text{-}O)(\mu\text{-}1,2\text{-}O_2)(L)_2]^{2+}$ complexes of 6-Me_3TPA (tris(6-methyl-2-pyridylmethyl)amine)[34] and BnBQA (*N*-benzyl-*N*,*N*-bis(2-quinolinylmethyl)amine)[30] generated from the reactions of diiron(II) precursors with O_2 react with strong acid to generate nearly isotropic EPR signals at g = 2. In the case of the BnBQA complex, ^{57}Fe hyperfine splitting of the g = 2 signal is observed when the complex is ^{57}Fe-enriched,

showing that the unpaired electron is associated with a (μ-oxo)diiron(III,IV) species.[30] In another example (along the pink path in Scheme 6), the reaction of stoichiometric H_2O_2 with $[Fe^{III}_2(\mu\text{-}O)(TPA^*)_2(OH)(OH_2)]^{3+}$ (TPA* = tris(4-methoxy-3,5-dimethyl-2-pyridylmethyl)amine) directly forms a diiron(IV) intermediate with an open O=Fe^{IV}–O–Fe^{IV}–OH core via a presumed but unobserved diferric-peroxo intermediate in ~70% yield.[69] Upon treatment with 1 eq. $HClO_4$, the nascent diiron(IV) complex converts into a complex with an $Fe^{IV}_2(\mu\text{-}O)_2$ diamond core. A fourth example (along the blue path in Scheme 6) describes the reaction of $[Fe^{III}_2(\mu\text{-}O)(6\text{-HPA})(OH_2)_2]^{4+}$ (6-HPA = 1,2-bis{2-[bis(2-pyridylmethyl)-aminomethyl]pyridin-6-yl}-ethane) with H_2O_2 and 2 eq. Et_3N to generate a (μ-oxo)(μ-1,2-peroxo)-diiron(III) derivative that is in equilibrium with a diiron(IV) intermediate with an O=Fe^{IV}–O–Fe^{IV}=O core.[54]

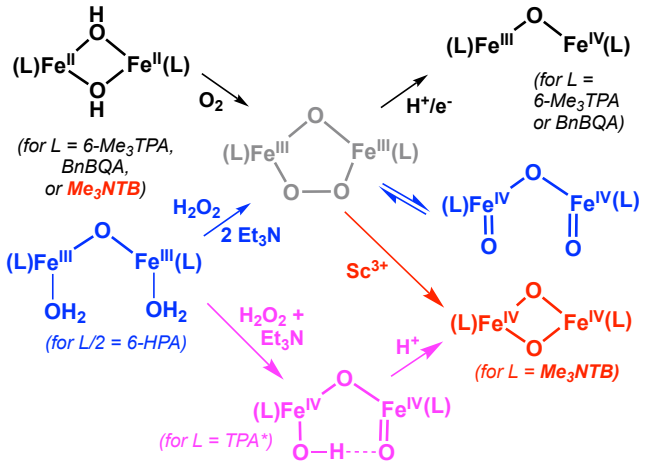

Scheme 6. Formation of high-valent diiron species from the reaction of a diiron(II) precursor with O_2 or a diiron(III) precursor with H_2O_2. For L = 6-Me_3TPA and BnBQA (black), an Fe^{III}–O–Fe^{IV} species is formed upon protonation of the peroxo intermediate.[30,32] For the dinucleating 6-HPA (blue), an O=Fe^{IV}–O–Fe^{IV}=O species is formed in equilibrium with the peroxo intermediate.[54] For L = TPA* (pink), an HO–Fe^{IV}–O–Fe^{IV}=O species is proposed to form from an unobserved (μ-oxo)(μ-1,2-hydroperoxo)diiron(III) species and then convert into an $Fe^{IV}_2(\mu\text{-}O)_2$ core upon protonation.[69] For L = Me_3NTB (red), a (μ-oxo)(μ-1,2-peroxo)diiron(III) intermediate **2** is formed upon exposure of its diiron(II) precursor to O_2 and is converted to **3**, a complex with an $Fe^{IV}_2(\mu\text{-}O)_2$ diamond core upon addition of Sc^{3+}.

In contrast, the formation of high-valent **3** from **2** (along the red path in Scheme 6) occurs by introducing Sc^{3+} (and not a proton), representing the first instance of a Lewis acid-mediated O–O bond cleavage in a diiron system. In fact, adding a Bronsted acid like $HClO_4$ or HOTf to **2** results in the protonation of its oxo bridge to form **2**+$\mathbf{H}^+$. These contrasting observations, with support from parallel theoretical calculations, show that Sc^{3+} preferentially attacks the peroxide bridge over the oxo bridge to promote O–O bond cleavage to generate **3**. However, the unique role of Sc^{3+} in this chemistry is nullified by the addition of excess water, which results in its hydrolysis to produce a proton that instead leads to the generation of **2**+$\mathbf{H}^+$. These results contrast the recent report that adding 1 eq of either $Sc(OTf)_3$ or $HClO_4$ to $[Fe^{III}(\beta\text{-BPMCN})(OOH)]^{2+}$ (where β-BPMCN = *cis*-β-bis(pyridyl-2-methyl)-*cis*-1,2-diaminocyclohexane) generates an oxidant capable of hydroxylating cyclohexane within seconds at -40 °C.[70] Browne and co-workers have also provided strong evidence that the $Sc(OTf)_3$-enhanced olefin epoxidation by the combination of $[Mn^{IV}_2(\mu\text{-}O)_3(tmtacn)_2]^{2+}$ (where tmtacn = 1,4,7-trimethyl-1,4,7-triazacyclononane) and H_2O_2 results from Bronsted acid formation upon hydrolysis of $Sc(OTf)_3$ by water present in the reaction mixture.[71] In contrast to these two examples, our system is unique in that the added acid (Bronsted or Lewis) has a choice between attacking the oxo bridge versus the peroxide bridge in a diiron model framework, resulting in significantly different outcomes from Bronsted and Lewis acids. Most importantly, our investigations into the conversion of **2** to **3** establish that both O atoms of one O_2 end up becoming incorporated into the high-valent diiron intermediate **3** (see, e. g., Scheme 1), thereby reproducing a key feature in the activation of O_2 by the diiron center of sMMO. Our investigation thus underscores the complexities of the chemistry involved in activating the peroxo O–O bond to generate high-valent oxidants in nonheme iron catalysts and highlights Nature's ability to deliver a key proton to a particular site in order to elicit a desired transformation.

Experimental Section

Materials and Physical Methods. Commercially available chemicals such as DBU (1,8-Diazabicyclo[5.4.0]undec-7-ene), Scandium triflate, Aluminium triflate, Yttrium triflate, perchloric acid, and solvents were used without further purification unless noted. $[Fe^{II}(Me_3NTB)(CH_3CN)](CF_3SO_3)_2$ (**1**) was synthesized as previously reported.[28] UV-vis absorption spectra were recorded with a HP 8453A diode array spectrophotometer equipped with a cryostat from UNISOKU Scientific Instruments, Japan. All UV-vis absorption experiments were carried out in 1-cm path length cuvettes. Resonance Raman spectra were obtained at -40 °C with excitation at 561 nm (50 mW at source, Cobolt Lasers) or 660 nm (100 mW at source, Cobolt Lasers) through the sample in a flat bottom NMR tube using a 90° scattering arrangement (parallel to the slit direction). Resonance Raman spectra on frozen samples (at 77 K) were obtained using a 135° back scattering arrangement. The collimated Raman scattering was collected using two Plano convex lenses (f = 12 cm, placed at an appropriate distance) through appropriate long pass edge filters (Semrock) into an Acton AM-506M3 monochromator equipped with a Princeton Instruments ACTON PyLON LN/CCD-1340x400 detector. The detector was cooled to -120 °C prior to the experiments. Spectral calibration was performed using the Raman spectrum of

acetonitrile/toluene 50:50 (v:v).[72] Each spectrum was accumulated, typically 60 times with 5 s acquisition time, resulting in a total acquisition time of 5 min per spectrum. The collected data was processed using Spekwin32,[73] and a multi-point baseline correction was performed for all spectra. Iron K-edge X-ray absorption spectra for **2** and **3** were collected on SSRL beamline 9–3 using a 100-element solid-state Ge detector (Canberra) with a SPEAR storage ring current of ~500 mA at a power of 3.0 GeV. The incoming X-rays were unfocused using a Si(220) double crystal monochromator, which was detuned to 70% of the maximal flux to attenuate harmonic X-rays. Between 6 and 8 scans of the fluorescence excitation spectra for each sample were collected from 6882 to 8000 eV at a temperature (10 K) that was controlled by an Oxford Instruments CF1208 continuous-flow liquid helium cryostat. An iron foil was placed in the beam pathway prior to the ionization chamber I_0 and scanned concomitantly for an energy calibration, with the first inflection point of the edge assigned to 7112.0 eV. A 3 μm, 6 μm or 9 μm Mn filter and a Soller slit were used to increase the signal-to-noise ratio of the spectra. Photoreduction was monitored by scanning the same spot on the sample twice and comparing the first derivative peaks associated with the edge energy during collection, but none was observed in the present study. The detector channels from the scans were examined, calibrated, averaged, and processed for EXAFS analysis using EXAFSPAK[74] to extract $\chi(k)$. Theoretical phase and amplitude parameters for a given absorber–scatterer pair were calculated using FEFF 8.40[75] and were utilized by the "opt" program of the EXAFSPAK package during curve fitting. In all analyses, the coordination number of a given shell was a fixed parameter and was varied iteratively in integer steps, while the bond lengths (R) and mean-square deviation (σ^2) were allowed to freely float. The amplitude reduction factor S_0 was fixed at 0.9, while the edge-shift parameter E_0 was allowed to float as a single value for all shells. Thus, in any given fit, the number of floating parameters was typically equal to (2 × num shells) + 1. The k range of the data is 2–14.5 $Å^{-1}$. The pre-edge analysis was performed on data normalized in the "process" program of the EXAFSPAK package, and pre-edge features were fit between 7108 and 7118 eV for all samples using the Fityk[76] program with pseudo-Voigt functions composed of 50:50 Gaussian/Lorentzian functions. Mössbauer spectra were recorded with two spectrometers using Janis Research (Wilmington, MA) SuperVaritemp dewars that allow studies in applied magnetic fields up to 8 T in the temperature range from 1.5 to 200 K. Mössbauer spectral simulations were performed using the WMOSS software package (SEE Co, Edina, MN)), all figures were generated by SpinCount.[77]

Sample preparation procedures. A 4 mM solution of **1** in CH_3CN or CD_3CN was prepared in a 1-cm cuvette in a nitrogen containing glovebox and 1.5 equivalents of DBU/H_2O is added to generate the putative diron(II) species [**1**+**DBU**] at -40 °C. At this stage, a balloon containing moisture-free oxygen gas is used to purge the headspace of the cuvette to carry out oxygen activation to 1produce a deep-green solution of $[Fe_2^{III}(\mu\text{-O})(\mu\text{-O}_2)(Me_3NTB)]^{3+}$(**2**). This process was monitored by UV-vis absorption spectroscopy. When the yield of **2** was maximized, pre-cooled pipettes were used to transfer the solution to a NMR tube and then frozen at 77K using liquid nitrogen for resonance raman studies. Similarly, for Mössbauer studies, a 2 mM solution of ^{57}Fe enriched **1** in CH_3CN was prepared in a nitrogen containing glovebox and to it 1.5 equivalents of DBU was added and then oxygenated to generate **2**. At this point, the solution was transferred to a Mossbauer cup and frozen at 77K using liquid nitrogen. For XAS studies, a 4 mM solution of **1** in CH_3CN was prepared in a nitrogen containing glovebox and was generated in a similar fashion, except the solution was frozen in an XAS cup.

Computational details. All DFT calculations were performed with the ADF program[78] (version 2017) with the S12g/TZ2P setup[62] including COSMO solvation and ZORA scalar relativistic corrections self-consistently. Full details can be found in the Supporting Information.

Supporting Information

The Supporting Information is available free of charge on the ACS Publications website at DOI: XXXXXXXX

Additional data, including Figures S1–S21 and Tables S1–S7 (PDF)

AUTHOR INFORMATION

Corresponding Author

*ysguo@andrew.cmu.edu
*larryque@umn.edu
*marcel.swart@gmail.com

ORCID
Lawrence Que, Jr.: 0000-0002-0989-2813
Saikat Banerjee: 0000-0003-0013-8037
Apparao Draksharapu: 0000-0001-7897-3230
Patrick Crossland: 0000-0001-7819-371X
Ruixi Fan: 0000-0002-6996-4276
Yisong Guo: 0000-0002-4132-3565
Marcel Swart: 0000-0002-8174-8488

Present Address

A. Draksharapu: Department of Chemistry, Indian Institute of Technology Kanpur, Kanpur 208016, India.

Notes
The authors declare no competing financial interests.

Acknowledgements

The authors are thankful for grants from the U. S. National Institutes of Health (R01 GM-38767 and R35 GM-131721 to L.Q.), the U. S. National Science Foundation (CHE1654060 to Y.G.), and MICINN (CTQ2017-87392-P to M.S.) for support of this work. XAS data were collected at the Stanford Synchrotron Radiation Lightsource Beamline 9-3. Use of the Stanford Synchrotron Radiation Lightsource, SLAC

National Accelerator Laboratory, is supported by the U.S. Department of Energy, Office of Science, Office of Basic Energy Sciences under Contract No. DE-AC02-76SF00515. The SSRL Structural Molecular Biology Program is supported by the DOE Office of Biological and Environmental Research, and by the National Institutes of Health, National Institute of General Medical Sciences (P41GM103393). The contents of this publication are solely the responsibility of the authors and do not necessarily represent the official views of NIGMS or NIH. We acknowledge several insightful discussions with Dr. Andrew Jasniewski that helped in developing the study presented here.

References

(1) Banerjee, R.; Jones, J. C.; Lipscomb, J. D. Soluble Methane Monooxygenase. *Annu. Rev. Biochem.* **2019**, *88* (1), 409–431.

(2) Jasniewski, A. J.; Que, L. Dioxygen Activation by Nonheme Diiron Enzymes: Diverse Dioxygen Adducts, High-Valent Intermediates, and Related Model Complexes. *Chem. Rev.* **2018**, *118* (5), 2554–2592.

(3) Trehoux, A.; Mahy, J. P.; Avenier, F. A Growing Family of O_2 Activating Dinuclear Iron Enzymes with Key Catalytic Diiron(III)-Peroxo Intermediates: Biological Systems and Chemical Models. *Coord. Chem. Rev.* **2016**, *322*, 142–158.

(4) Cotruvo, J. A.; Stubbe, J. Class I Ribonucleotide Reductases: Metallocofactor Assembly and Repair In Vitro and In Vivo. *Annu. Rev. Biochem.* **2011**, *80* (1), 733–767.

(5) Lee, S. K.; Nesheim, J. C.; Lipscomb, J. D. Transient Intermediates of the Methane Monooxygenase Catalytic Cycle. *J. Biol. Chem.* **1993**, *268* (29), 21569–21577.

(6) Liu, K. E.; Valentine, A. M.; Salifoglou, A.; Lippard, S. J.; Wang, D.; Huynh, B. H.; Edmondson, D. E. Kinetic and Spectroscopic Characterization of Intermediates and Component Interactions in Reactions of Methane Monooxygenase from Methylococcus Capsulatus (Bath). *J. Am. Chem. Soc.* **1995**, *117* (41), 10174–10185.

(7) Moënne-Loccoz, P.; Baldwin, J.; Ley, B. A.; Loehr, T. M.; Bollinger, J. M. O_2 Activation by Non-Heme Diiron Proteins: Identification of a Symmetric μ-1,2-Peroxide in a Mutant of Ribonucleotide Reductase. *Biochemistry* **1998**, *37* (42), 14659–14663.

(8) Baldwin, J.; Krebs, C.; Saleh, L.; Stelling, M.; Huynh, B. H.; Bollinger, J. M.; Riggs-Gelasco, P. Structural Characterization of the Peroxodiiron(III) Intermediate Generated during Oxygen Activation by the W48A/D84E Variant of Ribonucleotide Reductase Protein R2 from *Escherichia Coli*. *Biochemistry* **2003**, *42* (45), 13269–13279.

(9) Broadwater, J. A.; Ai, J.; Loehr, T. M.; Sanders-Loehr, J.; Fox, B. G. Peroxodiferric Intermediate of Stearoyl-Acyl Carrier Protein Δ^9 Desaturase: Oxidase Reactivity during Single Turnover and Implications for the Mechanism of Desaturation. *Biochemistry* **1998**, *37* (42), 14664–14671.

(10) Broadwater, J. A.; Achim, C.; Münck, E.; Fox, B. G. Mössbauer Studies of the Formation and Reactivity of a Quasi-Stable Peroxo Intermediate of Stearoyl-Acyl Carrier Protein Δ^9-Desaturase. *Biochemistry* **1999**, *38* (38), 12197–12204.

(11) Vu, V. V.; Emerson, J. P.; Martinho, M.; Yeon, S. K.; Münck, E.; Myung, H. P.; Que, L. Human Deoxyhypusine Hydroxylase, an Enzyme Involved in Regulating Cell Growth, Activates O_2 with a Nonheme Diiron Center. *Proc. Natl. Acad. Sci. U. S. A.* **2009**, *106* (35), 14814–14819.

(12) Han, Z.; Sakai, N.; Böttger, L. H.; Klinke, S.; Hauber, J.; Trautwein, A. X.; Hilgenfeld, R. Crystal Structure of the Peroxo-Diiron(III) Intermediate of Deoxyhypusine Hydroxylase, an Oxygenase Involved in Hypusination. *Structure* **2015**, *23* (5), 882–892.

(13) Jasniewski, A. J.; Engstrom, L. M.; Vu, V. V.; Park, M. H.; Que, L. X-Ray Absorption Spectroscopic Characterization of the Diferric-Peroxo Intermediate of Human Deoxyhypusine Hydroxylase in the Presence of Its Substrate EIF5a. *J. Biol. Inorg. Chem.* **2016**, *21* (5–6), 605–618.

(14) Tong, W. H.; Chen, S.; Lloyd, S. G.; Edmondson, D. E.; Huynh, B. H.; Stubbe, J. Mechanism of Assembly of the Diferric Cluster-Tyrosyl Radical Cofactor of *Escherichia Coli* Ribonucleotide Reductase from the Diferrous Form of the R2 Subunit. *J. Am. Chem. Soc.* **1996**, *118* (8), 2107–2108.

(15) Sturgeon, B. E.; Burdi, D.; Chen, S.; Huynh, B. H.; Edmondson, D. E.; Stubbe, J. A.; Hoffman, B. M. Reconsideration of X, the Diiron Intermediate Formed during Cofactor Assembly in *E. Coli* Ribonucleotide Reductase. *J. Am. Chem. Soc.* **1996**, *118* (32), 7551–7557.

(16) Burdi, D.; Willems, J. P.; Riggs-Gelasco, P.; Antholine, W. E.; Stubbe, J.; Hoffman, B. M. The Core Structure of X Generated in the Assembly of the Diiron Cluster of Ribonucleotide Reductase: $^{17}O_2$ and $H_2{}^{17}O$ ENDOR. *J. Am. Chem. Soc.* **1998**, *120* (49), 12910–12919.

(17) Lee, S. K.; Lipscomb, J. D. Oxygen Activation Catalyzed by Methane Monooxygenase Hydroxylase Component: Proton Delivery during the O-O Bond Cleavage Steps. *Biochemistry* **1999**, *38* (14), 4423–4432.

(18) Tinberg, C. E.; Lippard, S. J. Revisiting the Mechanism of Dioxygen Activation in Soluble Methane Monooxygenase from M. Capsulatus (Bath): Evidence for a Multi-Step, Proton-Dependent Reaction Pathway. *Biochemistry* **2009**, *48* (51), 12145–12158.

(19) Banerjee, R.; Proshlyakov, Y.; Lipscomb, J. D.; Proshlyakov, D. A. Structure of the Key Species in the Enzymatic Oxidation of Methane to Methanol. *Nature* **2015**, *518* (7539), 431–434.

(20) Tshuva, E. Y.; Lippard, S. J. Synthetic Models for Non-Heme Carboxylate-Bridged Diiron Metalloproteins: Strategies and Tactics. *Chem. Rev.* **2004**, *104* (2), 987–1012.

(21) Dong, Y.; Ménage, S.; Brennan, B. A.; Elgren, T. E.; Jang, H. G.; Pearce, L. L.; Que, L. Dioxygen Binding to Diferrous Centers. Models for Diiron-Oxo Proteins. *J. Am. Chem. Soc.* **1993**, *115* (5), 1851–1859.

(22) Dong, Y.; Yan, S.; Young, V. G.; Que, L. Crystal Structure Analysis of a Synthetic Non-Heme Diiron—O_2 Adduct: Insight into the Mechanism of Oxygen Activation. *Angew. Chem. Int. Ed.* **1996**, *35* (6), 618–620.

(23) Ookubo, T.; Sugimoto, H.; Nagayama, T.; Masuda, H.; Sato, T.; Tanaka, K.; Maeda, Y.; Okawa, H.; Hayashi, Y.; Uehara, A.; Suzuki, M. *cis*-μ-1,2-Peroxo Diiron Complex: Structure and Reversible Oxygenation. *J. Am. Chem. Soc.* **1996**, *118* (3), 701–702.

(24) Yamashita, M.; Furutachi, H.; Tosha, T.; Fujinami, S.; Saito, W.; Maeda, Y.; Takahashi, K.; Tanaka, K.; Kitagawa, T.; Suzuki, M. Regioselective Arene Hydroxylation Mediated by a (μ-Peroxo)Diiron(III) Complex: A Functional Model for Toluene Monooxygenase. *J. Am. Chem. Soc.* **2007**, *129* (1), 2–3.

(25) Frisch, J. R.; Vu, V. V.; Martinho, M.; Münck, E.; Que, L. Characterization of Two Distinct Adducts in the Reaction of a Nonheme Diiron(II) Complex with O_2. *Inorg. Chem.* **2009**, *48* (17), 8325–8336.

(26) Pap, J. S.; Draksharapu, A.; Giorgi, M.; Browne, W. R.; Kaizer, J.; Speier, G. Stabilisation of μ-Peroxido-Bridged Fe(III) Intermediates with Non-Symmetric Bidentate N-Donor Ligands. *Chem. Comm.* **2014**, *50* (11), 1326–1329.

(27) Sekino, M.; Furutachi, H.; Tojo, R.; Hishi, A.; Kajikawa, H.; Suzuki, T.; Suzuki, K.; Fujinami, S.; Akine, S.; Sakata, Y.; Ohta, T.; Hayami, S.; Suzuki, M. New Mechanistic Insights into Intramolecular Aromatic Ligand Hydroxylation and Benzyl Alcohol Oxidation Initiated by the Well-Defined (μ-Peroxo)Diiron(III) Complex. *Chem. Comm.* **2017**, *53* (63),

8838–8841.
(28) Seo, M. S.; Kim, N. H.; Cho, K. Bin; So, J. E.; Park, S. K.; Clémancey, M.; Garcia-Serres, R.; Latour, J. M.; Shaik, S.; Nam, W. A Mononuclear Nonheme Iron(IV)-Oxo Complex Which Is More Reactive than Cytochrome P450 Model Compound I. *Chem. Sci.* **2011**, *2* (6), 1039–1045.
(29) Kryatov, S. V.; Taktak, S.; Korendovych, I. V.; Rybak-Akimova, E. V.; Kaizer, J.; Torelli, S.; Shan, X.; Mandal, S.; MacMurdo, V. L.; Mairata I Payeras, A.; Que, L. Dioxygen Binding to Complexes with $Fe^{II}_2(\mu\text{-}OH)_2$ Cores: Steric Control of Activation Barriers and O_2-Adduct Formation. *Inorg. Chem.* **2005**, *44* (1), 85–99.
(30) Cranswick, M. A.; Meier, K. K.; Shan, X.; Stubna, A.; Kaizer, J.; Mehn, M. P.; Münck, E.; Que, L. Protonation of a Peroxodiiron(III) Complex and Conversion to a Diiron(III/IV) Intermediate: Implications for Proton-Assisted O-O Bond Cleavage in Nonheme Diiron Enzymes. *Inorg. Chem.* **2012**, *51* (19), 10417–10426.
(31) Sanders-Loehr, J.; Wheeler, W. D.; Shiemke, A. K.; Averill, B. A.; Loehr, T. M. Electronic and Raman Spectroscopic Properties of Oxo-Bridged Dinuclear Iron Centers in Proteins and Model Compounds. *J. Am. Chem. Soc.* **1989**, *111* (21), 8084–8093.
(32) Fiedler, A. T.; Shan, X.; Mehn, M. P.; Kaizer, J.; Torelli, S.; Frisch, J. R.; Kodera, M.; Que, L. Spectroscopic and Computational Studies of (μ-Oxo)(μ-1,2-Peroxo)Diiron(III) Complexes of Relevance to Nonheme Diiron Oxygenase Intermediates. *J. Phys. Chem. A* **2008**, *112* (50), 13037–13044.
(33) Kodera, M.; Taniike, Y.; Itoh, M.; Tanahashi, Y.; Shimakoshi, H.; Kano, K.; Hirota, S.; Iijima, S.; Ohba, M.; Okawa, H. Synthesis, Characterization, and Activation of Thermally Stable μ-1,2-Peroxodiiron(III) Complex. *Inorg. Chem.* **2001**, *40* (19), 4821–4822.
(34) Dong, Y.; Zang, Y.; Shu, L.; Wilkinson, E. C.; Que, L.; Kauffmann, K.; Münck, E. Models for Nonheme Diiron Enzymes. Assembly of a High-Valent $Fe_2(\mu\text{-}O)_2$ Diamond Core from Its Peroxo Precursor. *J. Am. Chem. Soc.* **1997**, *119* (51), 12683–12684.
(35) Zhang, X.; Furutachi, H.; Fujinami, S.; Nagatomo, S.; Maeda, Y.; Watanabe, Y.; Kitagawa, T.; Suzuki, M. Structural and Spectroscopic Characterization of (μ-Hydroxo or μ-Oxo)(μ-Peroxo)Diiron(III) Complexes: Models for Peroxo Intermediates of Non-Heme Diiron Proteins. *J. Am. Chem. Soc.* **2005**, *127* (3), 826–827.
(36) Zheng, H.; Zang, Y.; Dong, Y.; Young, V. G.; Que, L. Complexes with $Fe^{III}_2(\mu\text{-}O)(\mu\text{-}OH)$, $Fe^{III}_2(\mu\text{-}O)_2$, and $[Fe^{III}_3(\mu_2\text{-}O)_3]$ Cores: Structures, Spectroscopy, and Core Interconversions. *J. Am. Chem. Soc.* **1999**, *121* (10), 2226–2235.
(37) Hsu, H. F.; Dong, Y.; Shu, L.; Young, V. G.; Que, L. Crystal Structure of a Synthetic High-Valent Complex with an $Fe_2(\mu\text{-}O)_2$ Diamond Core. Implications for the Core Structures of Methane Monooxygenase Intermediate Q and Ribonucleotide Reductase Intermediate X. *J. Am. Chem. Soc.* **1999**, *121* (22), 5230–5237.
(38) Skulan, A. J.; Hanson, M. A.; Hsu, H. F.; Que, L.; Solomon, E. I. Spectroscopic Study of $[Fe_2O_2(5\text{-}Et_3\text{-}TPA)_2]^{3+}$: Nature of the Fe_2O_2 Diamond Core and Its Possible Relevance to High-Valent Binuclear Non-Heme Enzyme Intermediates. *J. Am. Chem. Soc.* **2003**, *125* (24), 7344–7356.
(39) Xue, G.; Wang, D.; De Hont, R.; Fiedler, A. T.; Shan, X.; Munck, E.; Que, L. A Synthetic Precedent for the $[Fe^{IV}_2(\mu\text{-}O)_2]$ Diamond Core Proposed for Methane Monooxygenase Intermediate Q. *Proc. Natl. Acad. Sci.* **2007**, *104* (52), 20713–20718.
(40) Zang, Y.; Dong, Y.; Que, L.; Kauffmann, K.; Münck, E. The First Bis(μ-Oxo)Diiron (III) Complex. Structure and Magnetic Properties of $[Fe_2(\mu\text{-}O)_2(6TLA)_2](ClO_4)_2$. *J. Am. Chem. Soc.* **1995**, *117* (3), 1169–1170.
(41) Wilkinson, E. C. Raman Signature of the Fe_2O_2 "diamond" Core. *J. Am. Chem. Soc.* **1998**, *120* (5), 955–962.
(42) Lõkov, M.; Tshepelevitsh, S.; Heering, A.; Plieger, P. G.; Vianello, R.; Leito, I. On the Basicity of Conjugated Nitrogen Heterocycles in Different Media. *Eur. J. Org. Chem.* **2017**, *30* (30), 4475–4489.
(43) Que, Jr., L.; Tolman, W. B.; Que Jr., L.; Tolman, W. B. Bis(μ-Oxo)Dimetal "Diamond" Cores in Copper and Iron Complexes Relevant to Biocatalysis. *ChemInform* **2010**, *33* (29), no-no.
(44) Cutsail, G. E.; Banerjee, R.; Zhou, A.; Que, L.; Lipscomb, J. D.; Debeer, S. High-Resolution Extended X-Ray Absorption Fine Structure Analysis Provides Evidence for a Longer Fe···Fe Distance in the Q Intermediate of Methane Monooxygenase. *J. Am. Chem. Soc.* **2018**, *140* (48), 16807–16820.
(45) Que, L. Physical Methods in Bioinorganic Chemistry: Spectroscopy and Magnetism; University Science Books: Sausalito, Calif., 2000.
(46) Fukuzumi, S.; Ohkubo, K. Quantitative Evaluation of Lewis Acidity of Metal Ions Derived from the *g* Values of ESR Spectra of Superoxide: Metal Ion Complexes in Relation to the Promoting Effects in Electron Transfer Reactions. *Chem. Eur. J.* **2000**, *6* (24), 4532–4535.
(47) Fukuzumi, S.; Ohkubo, K. Fluorescence Maxima of 10-Methylacridone-Metal Ion Salt Complexes: A Convenient and Quantitative Measure of Lewis Acidity of Metal Ion Salts. *J. Am. Chem. Soc.* **2002**, *124* (35), 10270–10271.
(48) Sankaralingam, M.; Lee, Y. M.; Pineda-Galvan, Y.; Karmalkar, D. G.; Seo, M. S.; Jeon, S. H.; Pushkar, Y.; Fukuzumi, S.; Nam, W. Redox Reactivity of a Mononuclear Manganese-Oxo Complex Binding Calcium Ion and Other Redox-Inactive Metal Ions. *J. Am. Chem. Soc.* **2019**, *141* (3), 1324–1336.
(49) Li, F.; Van Heuvelen, K. M.; Meier, K. K.; Münck, E.; Que, L. Sc^{3+}-Triggered Oxoiron(IV) Formation from O_2 and Its Non-Heme Iron(II) Precursor via a Sc^{3+}–Peroxo–Fe^{3+} Intermediate. *J. Am. Chem. Soc.* **2013**, *135* (28), 10198–10201.
(50) Lee, Y. M.; Bang, S.; Kim, Y. M.; Cho, J.; Hong, S.; Nomura, T.; Ogura, T.; Troeppner, O.; Ivanović-Burmazović, I.; Sarangi, R.; Fukuzumi, S.; Nam, W. A Mononuclear Nonheme Iron(III)-Peroxo Complex Binding Redox-Inactive Metal Ions. *Chem. Sci.* **2013**, *4* (10), 3917–3923.
(51) Bang, S.; Lee, Y. M.; Hong, S.; Cho, K. Bin; Nishida, Y.; Seo, M. S.; Sarangi, R.; Fukuzumi, S.; Nam, W. Redox-Inactive Metal Ions Modulate the Reactivity and Oxygen Release of Mononuclear Non-Haem Iron(III)-Peroxo Complexes. *Nat. Chem.* **2014**, *6* (10), 934–940.
(52) Balch, A. L. The Reactivity of Spectroscopically Detected Peroxy Complexes of Iron Porphyrins. *Inorg. Chim. Acta.* **1992**, *198–200*, 297–307.
(53) Kodera, M.; Kawahara, Y.; Hitomi, Y.; Nomura, T.; Ogura, T.; Kobayashi, Y. Reversible O–O Bond Scission of Peroxodiiron(III) to High-Spin Oxodiiron(IV) in Dioxygen Activation of a Diiron Center with a Bis-Tpa Dinucleating Ligand as a Soluble Methane Monooxygenase Model. *J. Am. Chem. Soc.* **2012**, *134* (32), 13236–13239.
(54) Kodera, M.; Ishiga, S.; Tsuji, T.; Sakurai, K.; Hitomi, Y.; Shiota, Y.; Sajith, P. K.; Yoshizawa, K.; Mieda, K.; Ogura, T. Formation and High Reactivity of the Anti-Dioxo Form of High-Spin μ-Oxodioxodiiron(IV) as the Active Species That Cleaves Strong C-H Bonds. *Chem. Eur. J.* **2016**, *22* (17), 5924–5936.
(55) Liu, L. V.; Hong, S.; Cho, J.; Nam, W.; Solomon, E. I. Comparison of High-Spin and Low-Spin Nonheme Fe^{III}-OOH Complexes in O-O Bond Homolysis and H-Atom Abstraction Reactivities. *J. Am. Chem. Soc.* **2013**, *135* (8), 3286–3299.
(56) Kaizer, J.; Costas, M.; Que, L. A Dramatic Push Effect on the Homolysis of Fe^{III}(OOR) Intermediates to Form Non-Heme Fe^{IV}=O Complexes. *Angew. Chem. Int. Ed.* **2003**, *42* (31), 3671–3673.
(57) Mairata i Payeras, A.; Ho, R. Y. N.; Fujita, M.; Que, L. The Reaction of $[Fe^{II}(Tpa)]$ with H_2O_2 in Acetonitrile and Acetone—Distinct Intermediates and Yet Similar Catalysis.

Chem. Eur. J. **2004**, *10* (20), 4944–4953.
(58) Oloo, W. N.; Fielding, A. J.; Que, L. Rate-Determining Water-Assisted O-O Bond Cleavage of an Fe^{III}-OOH Intermediate in a Bio-Inspired Nonheme Iron-Catalyzed Oxidation. *J. Am. Chem. Soc.* **2013**, *135* (17), 6438–6441.
(59) Li, F.; Meier, K. K.; Cranswick, M. A.; Chakrabarti, M.; Van Heuvelen, K. M.; Münck, E.; Que, L. Characterization of a High-Spin Non-Heme Fe^{III}-OOH Intermediate and Its Quantitative Conversion to an Fe^{IV}=O Complex. *J. Am. Chem. Soc.* **2011**, *133* (19), 7256–7259.
(60) Halfen, J. A.; Mahapatra, S.; Wilkinson, E. C.; Kaderli, S.; Young, V. G.; Que, L.; Zuberbühler, A. D.; Tolman, W. B. Reversible Cleavage and Formation of the Dioxygen O-O Bond within a Dicopper Complex. *Science* **1996**, *271* (5254), 1397–1400.
(61) Cahoy, J.; Holland, P. L.; Tolman, W. B. Experimental Studies of the Interconversion of μ-H2:H2-Peroxo- and Bis(μ-Oxo)Dicopper Complexes. *Inorg. Chem.* **1999**, *38* (9), 2161–2168.
(62) Swart, M. A New Family of Hybrid Density Functionals. *Chem. Phys. Lett.* **2013**, *580*, 166–171.
(63) Swart, M.; Gruden, M. Spinning around in Transition-Metal Chemistry. *Acc. Chem. Res.* **2016**, *49* (12), 2690–2697.
(64) Honda, Y.; Arii, H.; Okumura, T.; Wada, A.; Funahashi, Y.; Ozawa, T.; Jitsukawa, K.; Masuda, H. Complexes with Fe^{III}_2(μ-O)(μ-OH) Core Surrounded by Hydrogen-Bonding Interaction. *Bull. Chem. Soc. Jpn.* **2007**, *80* (7), 1288–1295.
(65) Bickelhaupt, F. M.; Houk, K. N. Analyzing Reaction Rates with the Distortion/Interaction-Activation Strain Model. *Angew. Chem. Int. Ed.* **2017**, *56* (34), 10070–10086.
(66) Xue, G.; De Hont, R.; Münck, E.; Que, L. Million-Fold Activation of the [Fe_2(μ-O)$_2$] Diamond Core for C–H Bond Cleavage. *Nat. Chem.* **2010**, *2* (5), 400–405.
(67) Biswas, A. N.; Puri, M.; Meier, K. K.; Oloo, W. N.; Rohde, G. T.; Bominaar, E. L.; Münck, E.; Que, L. Modeling TauD- J : A High-Spin Nonheme Oxoiron(IV) Complex with High Reactivity toward C–H Bonds. *J. Am. Chem. Soc.* **2015**, *137* (7), 2428–2431.
(68) Puri, M.; Que, L. Toward the Synthesis of More Reactive S = 2 Non-Heme Oxoiron(IV) Complexes. *Acc. Chem. Res.* **2015**, *48* (8), 2443–52.
(69) Xue, G.; Fiedler, A. T.; Martinho, M.; Munck, E.; Que, L. Insights into the P-to-Q Conversion in the Catalytic Cycle of Methane Monooxygenase from a Synthetic Model System. *Proc. Natl. Acad. Sci.* **2008**, *105* (52), 20615–20620.
(70) Kal, S.; Draksharapu, A.; Que, L. Sc^{3+}(or $HClO_4$) Activation of a Nonheme Fe^{III}-OOH Intermediate for the Rapid Hydroxylation of Cyclohexane and Benzene. *J. Am. Chem. Soc.* **2018**, *140* (17), 5798–5804.
(71) Steen, J. D.; Stepanovic, S.; Parvizian, M.; De Boer, J. W.; Hage, R.; Chen, J.; Swart, M.; Gruden, M.; Browne, W. R. Lewis versus Brønsted Acid Activation of a Mn(IV) Catalyst for Alkene Oxidation. *Inorg. Chem.* **2019**, *58* (21), 14924–14930.
(72) International, A. Standard Guide for Raman Shift Standards for Spectrometer Calibration. *ASTM International*. 2002, pp 1–11.
(73) Menges, F. "Spekwin32 – optical spectrscopy software", Version 1.72.1, 2016. http://www.effemm2.de/spekwin/.
(74) George, G. N. G. N. George, EXAFSPAK; Stanford Synchrotron Radiation Laboratory: Stanford Linear Accelerator Center, Stanford, CA. 2000.
(75) Ankudinov, A.; Ravel, B. Real-Space Multiple-Scattering Calculation and Interpretation of X-Ray-Absorption near-Edge Structure. *Phys. Rev. B - Condens. Matter Mater. Phys.* **1998**, *58* (12), 7565–7576.
(76) Wojdyr, M. Fityk: A General-Purpose Peak Fitting Program. *J. Appl. Crystallogr.* **2010**, *43* (5 PART 1), 1126–1128.
(77) Petasis, D. T.; Hendrich, M. P. Quantitative Interpretation of Multifrequency Multimode EPR Spectra of Metal Containing Proteins, Enzymes, and Biomimetic Complexes. *Methods Enzymol.* **2015**, *563*, 171–208.
(78) Baerends, E. J. and co-workers. ADF 2017.01, SCM, Theoretical Chemistry, Vrije Universiteit, Amsterdam, The Netherlands http://www.scm.com.

Insert Table of Contents artwork here